Received: 10 March 2021 | Accepted: 5 April 2021

DOI: 10.1002/prp2.783

ORIGINAL ARTICLE

Seeking the exclusive binding region of phenylalkylamine derivatives on human T-type calcium channels via homology modeling and molecular dynamics simulation approach

You Lu[1,2] | Ming Li[3] | Gi Young Lee[4] | Na Zhao[5] | Zhong Chen[1,2] | Andrea Edwards[1] | Kun Zhang[1,2]

[1]Department of Physics and Computer Science, Xavier University of Louisiana, New Orleans, LA, USA

[2]Bioinformatics Core of Xavier NIH RCMI Center of Cancer Research, Xavier University of Louisiana, New Orleans, LA, USA

[3]Department of Physiology SL-39, Tulane University, New Orleans, LA, USA

[4]Department of Microbiology and Immunology, College of Veterinary Medicine, Cornell University, Ithaca, NY, USA

[5]Key Laboratory in Software Engineering of Yunnan Province, School of Software, Yunnan University, Kunming, China

Correspondence
Kun Zhang, Computer Science Department, Xavier University of Louisiana, New Orleans, LA 70125, USA.
Email: kzhang@xula.edu

Na Zhao, Key Laboratory in Software Engineering of Yunnan Province, School of Software, Yunnan University, Kunming, China.
Email: zhaonayx@126.com

Funding Information
This work was partly supported by funding from the National Institutes of Health (NIH) grant U54MD007595. The contents are solely the responsibility of the authors and do not necessarily represent the official views of the NIH.

Abstract

Pharmaceutical features of phenylalkylamine derivatives (PAAs) binding to calcium channels have been studied extensively in the past decades. Only a few PAAs have the binding specificity on calcium channels, for example, NNC 55-0396. Here, we created the homology models of human $Ca_v3.2$, $Ca_v3.3$ and use them as a receptor on the rigid docking tests. The nonspecific calcium channel blocker mibefradil showed inconsistent docking preference across four domains; however, NNC 55-0396 had a unique binding pattern on domain II specifically. The subsequent molecular dynamics (MD) simulations identified that $Ca_v3.1$, $Ca_v3.2$, and $Ca_v3.3$ share domain II when Ca^{2+} appearing in the neighbor region of selective filters (SFs). Moreover, free-energy perturbation analysis suggests single mutation of lysine at P-loop domain III, or threonine at the P-loop domain II largely reduced the total amount of hydration-free energy in the system. All these findings suggest that P-loop and segment six domain II in the T-type calcium channels (TCCs) are crucial for attracting the PAAs with specificity as the antagonist.

KEYWORDS
homology modeling, phenylalkylamine, selective binding, T-type calcium channels, virtual drug screening

Abbreviations: EEF, external electric force field; FEP, free-energy perturbation; LCC, L-type calcium channel; MD, molecular dynamics; NNC 55-0396, (1S,2S)-2-(2-(N-[(3-benzoimidazol-2-yl)propyl]-N-methylamino)ethyl)-6-fluoro 1,2,3,4-tetrahydro-1-isopropyl-2-naphtyl cyclopropanecarboxylate dihydrochloride; PAAs, phenylalkylamine derivatives; PCA, principal component analysis; RMSD, root-mean-square-displacement; SF, selective filter; SMD, steering molecular dynamics; TCCs, T-type calcium channels.

1 | INTRODUCTION

T-type calcium channels (TCCs) belong to the one sort of voltage-dependent calcium channel family. They are known to be activated by membrane depolarization, conducting inward currents with a small single-channel conductance. Roles of TCCs in controlling the hormone and neurotransmitter release under various conditions have been extensively studied in the past decades.[1–5] The distribution of TCCs can be found in pancreatic β-cells,[6] heart,[7] and neuron cells.[8] In β-cells, overexpressed TCC increased $[Ca^{2+}]_i$ followed by generating frequent random calcium spikes.[9] Humans with gradually raised calcium concentration will more likely develop type 2 diabetes in later life.[10] In cardiomyocytes, the TCC currents significantly affect the later stage of the action potential.[11] In neuron cells, the development of chronic neuropathic pain due to spinal cord injury is contributed by the increased activity of TCCs.[12]

When the inhibitor binds to the calcium channel, it cuts down the Ca^{2+} pathway by allosterically changing the pore conformation or physical blocks in the pore as a plug.[13] As the earliest launched TCC inhibitor, mibefradil was initially developed for blocking L-type calcium channel (LCC) and showed the promising effect of blocking TCCs in vitro.[14] Such phenylalkylamine derivatives (PAAs) are more likely to behave as a physical plug when interacting with TCCs. Unfortunately, mibefradil was withdrawn from the market due to the interaction with other drugs due to its effect on P450.[15] Because phenylalkylamine-based TCC antagonists are derived from LCC blockers, only some of them have specificity to block the TCC in vivo.[14] Recently discovered drug Z944[16] showed an excellent specificity and potent to block the TCC for treating epilepsy[17] and neuronal pain.[18] In contrast to phenylalkylamines that physically block the pore, Z944 was reported to change the conformation of TCC by shifting the α to π helix at domain II and further shut down the calcium currents.[19]

In this study, we created two homology models for human $Ca_v3.2$ (UniProt id: O95180) and $Ca_v3.3$ (UniProt id: Q9P0X4) in terms of the structure of human $Ca_v3.1$ at apostate. A total of three TCC structures were used in subsequent molecular dynamics (MD) simulations. Mibefradil, NNC-55-0396 were selected as the representative ligands in the MD to mimic the real cases when TCCs interact with different sorts of an antagonist. Also, the external electric force field MD and steering MD simulation was utilized to find the pathway of Ca^{2+} permeation when it penetrates the channel pore with and without introducing the blockers.

2 | MATERIALS AND METHODS

2.1 | Protein comparative modeling

Two human TCC 3D structures (α_1H and α_1I) were created by using the comparative modeling package from Rosetta.[20] The Cryo-EM structure of human $Ca_v3.1$(PDB id: 6KZO) at the apostate was selected as input for Rosetta to create the homology model of α_1H and α_1I. The energy-based clustering method[21] was applied to categorize the predicted models before the quality evaluation process. To filter out the low quality of structure, PROCHECK[22] and WHATCHECK[23] were employed on clustered data. Finally, the structures that hold the lowest Rosetta energy score will be selected as targets for the next tests, that is, rigid docking and MD simulations.

2.2 | Rigid docking with selected PAAs

The 3D structure of mibefradil and NNC 55-0396 was downloaded from the PubChem online database. We used Open Babel[24] to convert the compound format and Frog[25] to find the coordinate of compound conformers in 3D space. To find out the possible binding sites between existing antagonists and TCCs, we used AutoDock Vina[26] to simulate the rigid docking process. The searching box was set at the center of the SF with the grid spacing 0.375 Å and 40 grid points along *X*, *Y*, and *Z* directions. The number of predict binding modes is set as 10, and the random seed number was set as −1460306363.

2.3 | MD simulations

2.3.1 | Ion channel membrane assembly

The CHARMM-GUI Membrane Builder[27] was used to build the membrane system. The missing residues were modeled by GalxyFill. The heterogeneous lipid bilayer was created by choosing phosphatidylcholine lipid and phosphatidylethanolamine lipid ratio as 2 over 1 on both inner and outer leaflets of the membrane. The water thickness was set as 22.5 Å. The system size along the *X* and *Y* dimensions is set as 120 Å. About 150 mM calcium chloride solution was added into the 3D rectangle computational domain. To generate the parameter and force field file for selected TCC blockers, the Ligand Reader and Modeler[28] was used. Overall, the system was formed as an isothermal-isobaric ensemble at temperature 310 K.

2.3.2 | Classic MD simulation

The force field to support all MD simulations was set as CHARMM36m. All MD productions were conducted on the precompiled NAMD-2.14b GPU-acceleration Linux version. Since MD cases prepared by CHARMM-GUI Membrane Builder need to be equilibrated before long-term standard running. The energy minimization process was performed under gradually reduced restrain forces over six-constitute steps. To keep the system stable, the integration time step was set as 2 femtoseconds (fs) for the first and second steps, then adjust to 1 fs for the others. As long-term standard MD production, the integration time step was set as 2 fs and the position and velocity of all atoms in the system will be recorded every 10 picoseconds (ps). The maximum periodic electrostatics calculation was based on the 1 Å grid size with periodic boundary conditions. To

calculate the nonbound interactions, a cutoff of 12 Å is used with switch distance 10 Å as input conditions for solving Langevin equations at temperature 310 K and 1 atm. For long-term production, the trajectory information was collected over 100 nanoseconds (ns) timescale with zero restrictions added to it.

2.3.3 | Simulation under the external electric force field

The Cryo-EM structure of human α_1G at the apo statue shows the opening channel pore without ligand binding. To simulate the open channel process, an external voltage was required to apply to the lipid membrane. The external electric potential E_z along L_z can be defined by the equation: $E_z = \frac{V}{L_z \times 43.17}$, where V = −60 mV[29,30] and L_z is the average length of TCCs in Z direction at the last 10 ns from standard MD simulation. The numerical value of 43.17 was the force conversion coefficient used by NAMD-2.14b. Total MD simulation time under −60 mV for all TCCs was set as 100 ns.

2.3.4 | Structure identification through RMSD

For all the MD simulation cases, the structure clustering analysis was conducted when the overall system reaches equilibrium, typically, in the last 50 ns. The optimized number of clusters for a given length of MD data was determined by a comparison of the clustering results from various methods.[31]

2.3.5 | Steering MD

To simulate the Ca^{2+} influx through the channel pore, the steering molecular dynamics (SMD) method was employed. The clustering analysis of external electrical force field simulation provided the three most typical conformations for running SMD. We picked up one Ca^{2+} which most close to the SF as a pulling target. Then we applied a constant pulling velocity: V = −4e−5 Å/fs with spring constant K = 4 kcal/mol Å along z direction for 3 ns simulation. To minimize the artificial impact from fixed atoms in SMD simulation, we fixed the C-alpha atoms at four geometrical symmetrical amino acids that away from channel pore, in which Pro^{116}, Pro^{849}, Gln^{1373}, and Val^{1704} for α_1G; Pro^{116}, Pro^{801}, Pro^{1316}, and Thr^{1635} for α_1H; Pro^{116}, Pro^{669}, Pro^{1213}, and Thr^{1526} for α_1I, respectively. With Tcl scripts to define all necessary parameters, the repeating rate of each structure was set as 20.

2.3.6 | Finding calcium ion interaction pathway

The trajectory files generated by NAMD over the entire time-span were analyzed in PyContact.[32] To find the interactions between Ca^{2+} and select molecules, the maximal interatomic distance for contact scoring was set as 5 Å, the cutoff angle for hydrogen bonds was set as 120°, and maximal distance between the hydrogen bond receptor and the H-atom was set as 2.5 Å. Accumulate score was used to evaluate the interaction strength between Ca^{2+} and selected molecular.

TABLE 1 Protein basic local alignment search tool (BLAST) results on the identity score of a given length of amino acids between template proteins and targets.

	H-Ca_v3.1 (full length)	R-Ca_v1.1 (full length)	Bac-Ca_vAb (full length)
H-Ca_v3.2	62.58%	31.47%	23.93%
H-Ca_v3.3	57.02%	31.09%	24.46%

Abbreviations: Bac-Ca_vAb (5KMH), bacterial Ca_vAb; H-Ca_v3.1, human Ca_v3.1; R-Ca_v1.1, rabbit Ca_v1.1 (3JBR).

2.3.7 | Free energy perturbation analysis

The alchemical free-energy perturbation (FEP) method[33] was used to estimate the influence of Gibbs-free energy by mutation of pre-identified binding associated amino acids.[19] K^{3p1462} and T^{2p921} at α_1G, K^{3p1405} and T^{2p784} at α_1H, and K^{3p1302} and T^{2p742} at α_1I are mutated into alanine. Two FEP simulations were conducted for molecular in vacuum or immersed in bulk water. In every simulation, 20 equally stratified external parameters λ[34] in the range [0, 1] were used to sample the energy variation in 50 ps with coupled intramolecular interactions. The net solvation free energy change was computed as follows: $\Delta\Delta G_{mutation} = \Delta G^2_{hydr} - \Delta G^1_{hydr}$, where ΔG^2_{hydr} is hydration energy in the solvation state and ΔG^1_{hydr} is the hydration energy at the isolate state. The results of FEP were processed by ParseFEP in VMD 1.9.3 at temperature 310 K, Gram–Charlier order at 3, with Gaussian approximation and BAR estimator.[35]

2.4 | Nomenclature of targets and ligands

Key protein targets and ligands in this article are hyperlinked to corresponding entries in http://www.guidetopharmacology.org, the common portal for data from the IUPHAR/BPS Guide to PHARMACOLOGY,[36] and are permanently archived in the Concise Guide to PHARMACOLOGY 2019/20.[37]

3 | RESULTS

3.1 | Homology modeling

Compare to other calcium channel templates, 6KZO returns the standard protein BLAST identity value as 62.58%, 57.02% for the full length of amino acid (AA) sequences (Table 1). We only considered amino acids aligned with 139 to 1906 to generate the homology model for α_1H and α_1I to reduce the computational cost. The detailed alignment of amino acids for three TCC can be found in the supporting

information (Figure S1). Based on the target protein AA sequences, the energy-based clustering method has identified 10 and 19 featured structures for α_1H and α_1I, respectively. The Rosetta Comparative Modeling method uses the continuous alignment results of α_1H and α_1I to α_1G for generating the homology models. The AAs that are not included in 6KZO will affect the quality of predicted protein structures. We found that after trimmed these regions out, the highest Ramachandran *Z*-score can go to 99.5% (Figure 1A1), and side-chain planarity can reach 0.42 for selected α_1H homology modeling result (Figure 1A2). Meanwhile, the highest *Z*-score and side-chain planarity is 99.7% (Figure 1B1) and 0.425 for trimmed α_1I homology modeling results. The full structure comparison before and after trimmed for the unnecessary region of α_1H and α_1I is summarized in Table S1.

3.2 | Rigid docking with selected PAAs

Vina virtual screening process finds a similar binding pattern between receptor and ligands. The hydroxy-group of S^{4p1776} domain IV at α_1G forms hydrogen bonds with a hydrogen atom at ammonia

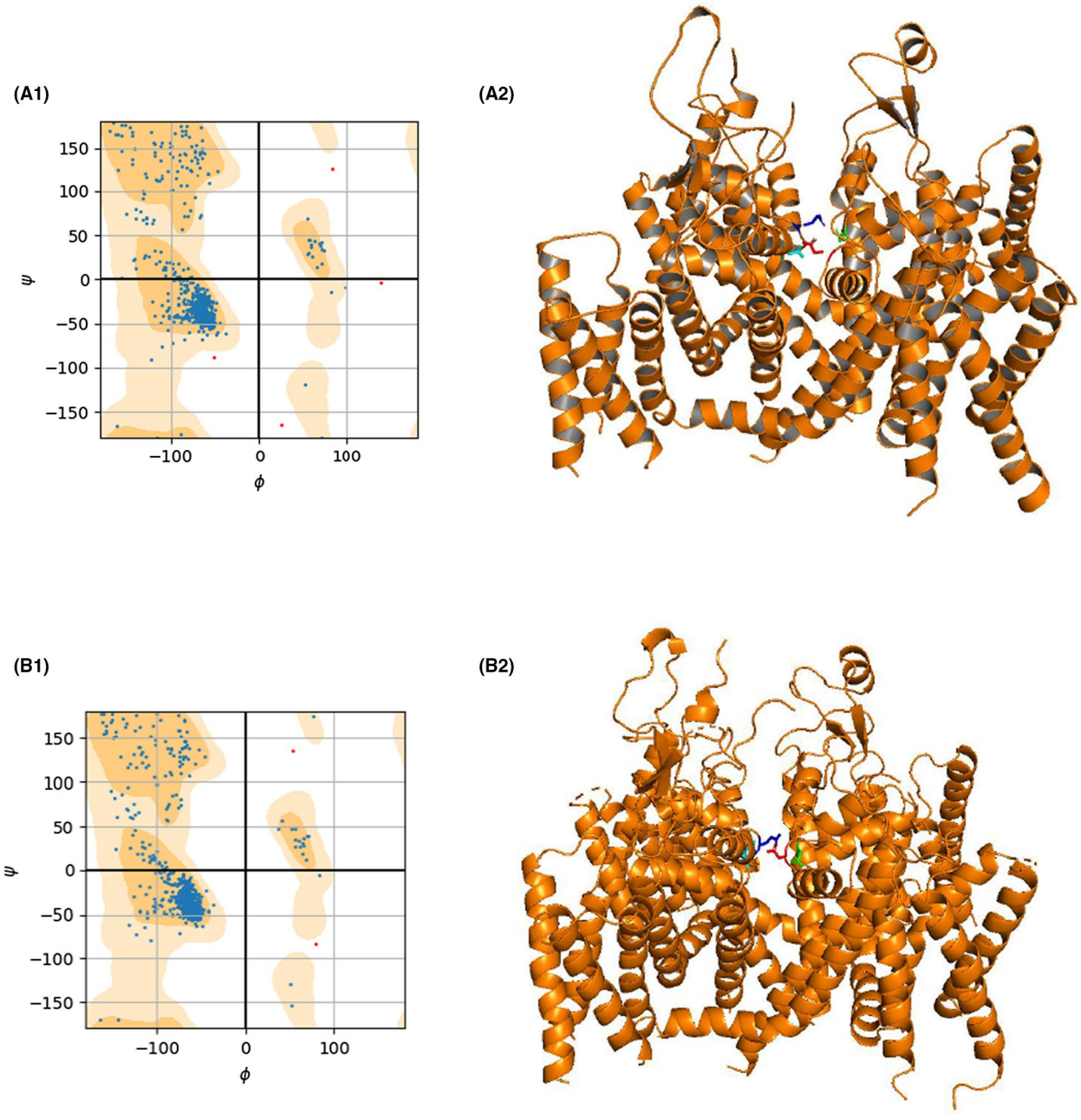

FIGURE 1 The distribution of torsional angles phi (ϕ) and psi (ψ) indicates over 99% of residues following in the favored region. (A1): the Ramachandran plot of selected α_1H model and (B1): the Ramachandran plot of selected α_1I model. The homology modeling of α_1H (A2) and α_1I (B2) structure show structural similarity to the template α_1G. The nonpolarized side-chain of SFs from the domain I to IV are colored as cyan, blue, green, and red.

(N_3) on the imidazole ring in the benzimidazole moiety of mibefradil. One hydrogen atom from the central ammonium of NNC 55-0396 could also form a hydrogen bond with carbonyl-oxygen in the amide of N^{2p952} domain II at α_1G (Figure 2A); For α_1H, one oxygen from carboxyl groups on the side-chain of mibefradil forms a hydrogen bond within 3.5 Å at S^{4p1707} from domain IV. Ammonia (N_3) on the imidazole ring in the benzimidazole moiety of NNC 55-0396 generates a connection with hydrogen atom from K^{3p1405} from domain III (Figure 2B); For α_1I, one hydrogen atom from ammonia (N_3) on the imidazole ring in the benzimidazole moiety of NNC 55-0396 could bind to the lipophilic side-chain of L^{2p776} at domain II. In comparison, the mibefradil is less likely to place at the center of the channel pore after binding to the amino acid (Figure 2C). The predicted binding affinities between testing drugs and TCCs from 2.67 to 25.99 mM (Figure 2D) are matched to other published studies.[14,38–40]

3.3 | MD simulations and analysis

The time-dependent root-mean-square-displacement (RMSD) plot for C-alpha and whole protein indicates that all three TCC membrane protein complex reaches the equilibrium at 20 ns (Figure 3A–α_1G, Figure S2A–α_1H, and Figure S3A–α_1I). Employing the first-five ranking eigenvalue,[41] the structural variation and conformation

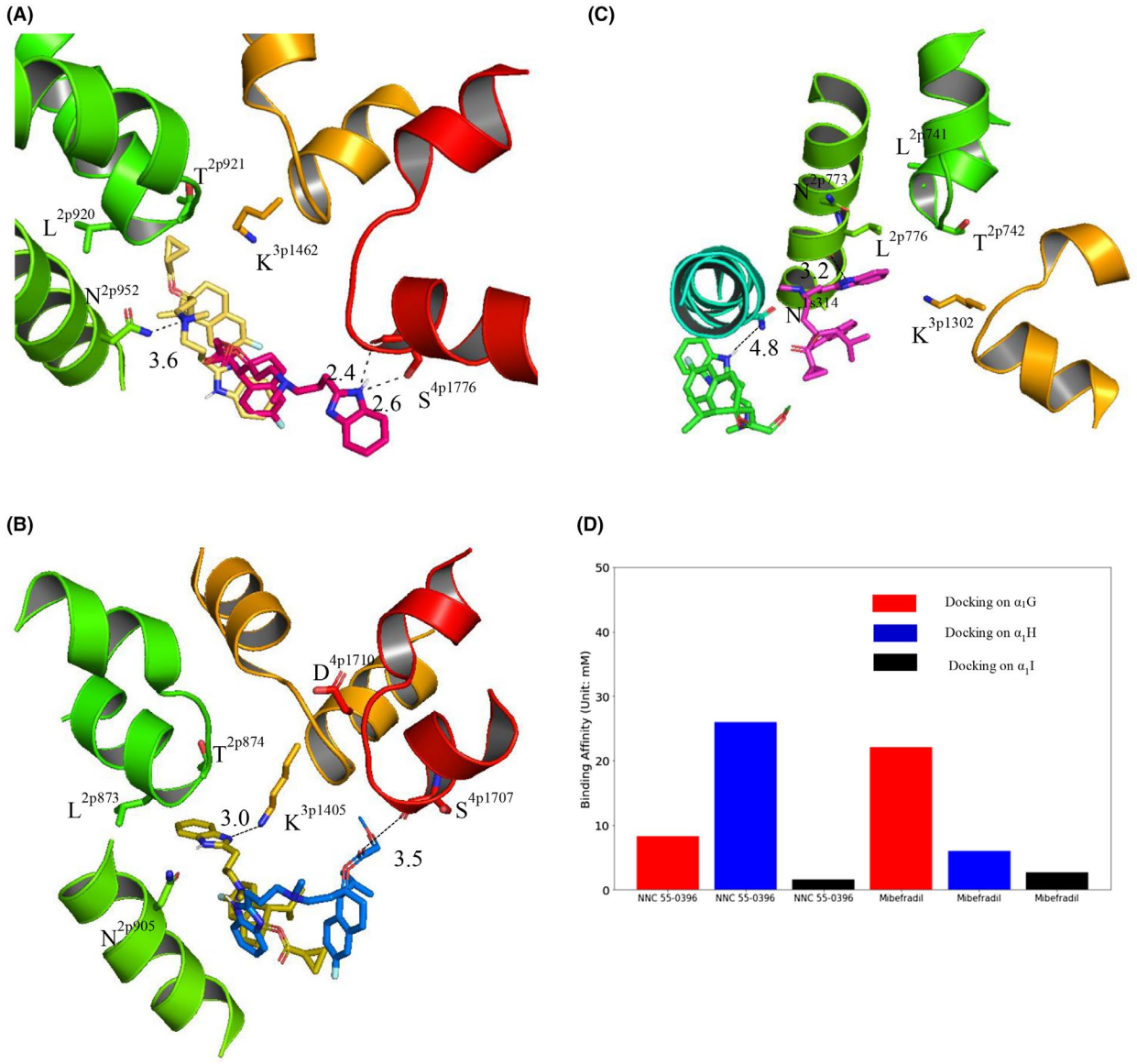

FIGURE 2 Comparison of amino acid binding sites between mibefradil and NNC 55-0396 across three T-type calcium channel (TCC) structures. Cyan: domain I; green: domain II; yellow: domain III; and red: domain IV. Sidechains of four key amino acids are given with partially displayed domains for better visualization. (A) mibefradil (magenta) binds to S^{4p1776} and NNC 55-0396 (wheat) binds to N^{2p952} at α_1G; (B) mibefradil (marine) binds to S^{4p1707} and NNC 55-0396 (yellow) binds to K^{3p1405} at α_1H; (C) mibefradil (green) binds to N^{1s314} and NNC 55-0396 (violet) binds to L^{2p776} at α_1I. (D) predict the binding affinity of mibefradil and NNC 55-0396 varied across α_1G (red), α_1H (blue), and α_1I (black) (unit: kcal/mol).

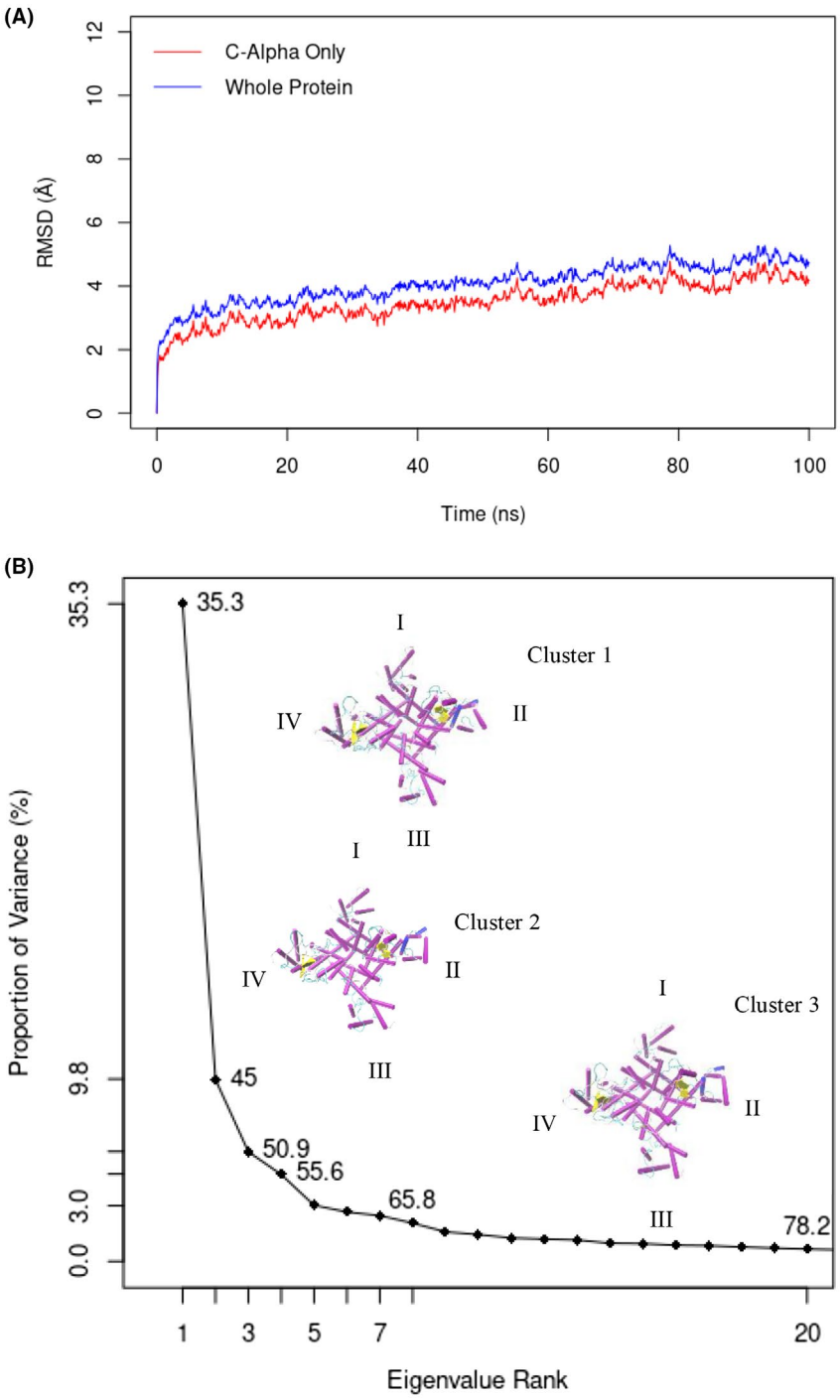

FIGURE 3 Structure variation of a_1G during the standard molecular dynamics (MD) simulation. (A) Comparison of the variation of root-mean-square-displacement (RMSD) over time between C-alpha and whole protein during 100 ns; (B) principal component analysis (PCA) analysis on MD data from 50 to 100 ns.

changes among α_1G, α_1H, and α_1I are 55.6% (Figure 4B), 61.6% (Figure S2B), and 56.5% (Figure S3B), respectively, while the proportion of variance decreasing monotonically with increased eigenvectors. For the first-three ranking eigenvalue, 50.9% α_1G structure was covered. And this number increased to 58.2% on α_1H and 51.4% on α_1I. Conducting principal component analysis (PCA) with three eigenvectors, we did not observe significant conformation changes in the transmembrane part at the last 50 ns simulation for all three TCC structures. The local structural differences among each cluster can be quickly distinguished by checking the shape of the transmembrane region between segment 5 and segment 6 (Figure 3B, clusters 1–3; Figure S2B, clusters 1–3; Figure S3B, clusters 1–3). For α_1G, expect for P-loop domain I which dynamic behavior is represented by high RMSD value, the rest of the domains have almost identical structure variation patterns in both sorted and unsorted trajectory data within 50 ns (Figure S4A); There is no clear structure variation of P-loop domains I and IV for α_1H till the last 5 ns (Figure S4A); For α_1I, P-loop domain IV has more unstable local fluctuations than other domains (Figure S4C).

The classic MD simulation (0–100 ns) with the following EEF MD (100–200 ns) simulation did not detect the penetration of

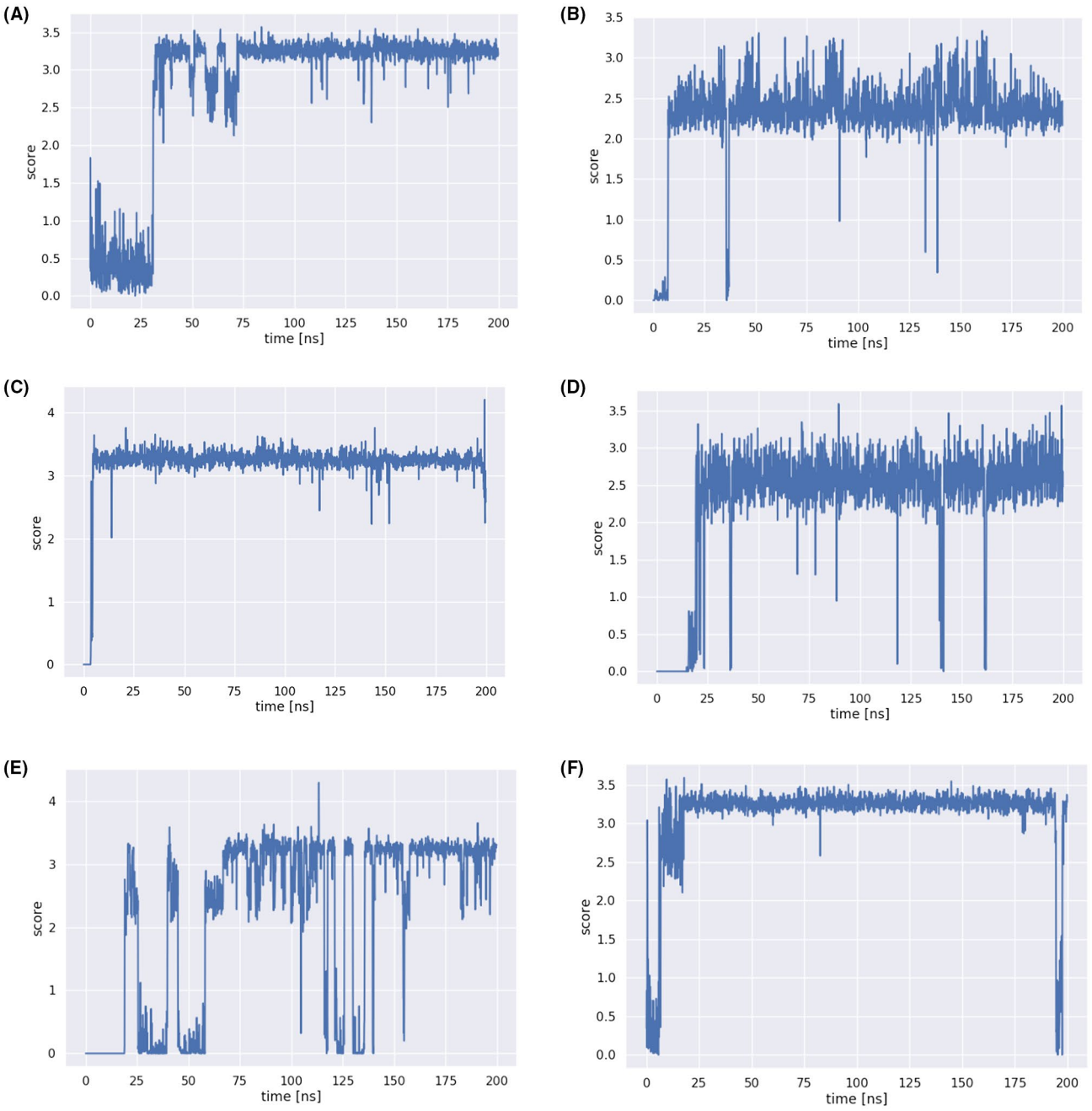

FIGURE 4 Combine the standard molecular dynamics (MD) simulation (0–100 ns) and external electric force field (EEF) MD simulation (100–200 ns) results show two extracellular Ca^{2+} ions that are attracted by two selected filters. (A) Ca^{37} binds to E^{1p354} at domain I since t = 30 ns (α_1G); (B) Ca^{15} binds to E^{2p923} at domain II at t = 8 ns (α_1G); (C) Ca^{58} binds to E^{1p280} at domain I (α_1H); (D) Second Ca^{38} binds to E^{2p876} at domain II (α_1H); (E) First Ca^{31} binds to E^{2p744} at domain II (α_1I); (F) Second Ca^{56} binds to E^{4p1601} at domain IV (α_1I).

calcium ion through the membrane in α_1G, α_1H, and α_1I. For α_1G, Ca^{37} binds to E^{1p354} domain I at t = 30 ns (Figure 4A), and Ca^{15} binds to E^{2p923} domain II at t = 8 ns (Figure 4B). Before simulation reaches steady-state, Ca^{37} is initially shared by two SFs at domains II and III for 25 ns, then it jumps to E^{1p354} domain I (Figure S5A and B). SF at domain IV has less attraction to calcium ions. For α_1H, Ca^{58} binds to E^{1p280} domain I at t = 0 (Figure 4C) and Ca^{38} binds to E^{2p876} domain II after 25 ns (Figure 4D). SF D^{3p1406} at domain III and D^{4p1710} at domain IV show limited binding affinity to Ca^{2+} (Figure S5C and D). For α_1I, Ca^{31} binds to E^{2p744} at domain II (Figure 4E) with unstable binding behavior and Ca^{56} firmly binds to E^{4p1601} domain IV (Figure 4F) after 25 ns. The SF at domains I and III shows fewer interests in binding Ca^{2+} (Figure S5E and F). At the end of EEF MD simulation, α_1G and α_1H have two calcium ions bind to the domaind I and II (Figure 5A and B); however, two calcium ions go to domains II and IV at α_1I (Figure 5C).

Charged amino acids or amino acids with polarity potential are more likely to interact with the Ca^{2+} when the interatomic distance

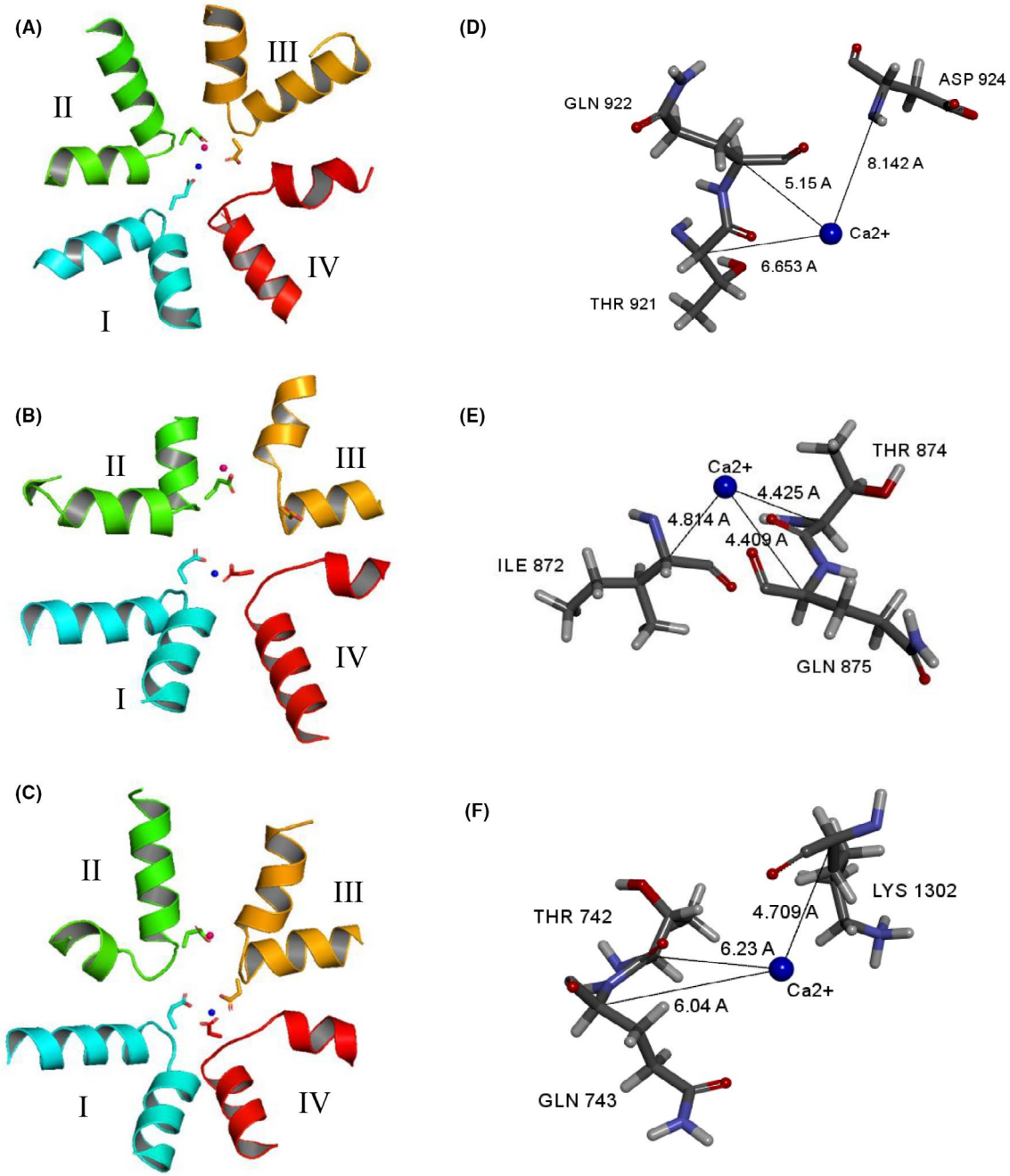

FIGURE 5 Interaction between Ca^{2+} and amino acids in the channel pore. The nonpolar side-chain of four SFs from domains I—IV are given as color order: cyan (domain I), green (domain II), yellow (domain III), and red (domain IV); (A and B) Ca^{2+} (blue dot) contacts to SF domain I and another Ca^{2+} (hotpink) contacts to SF domain II for α_1G and α_1H at the end of external electric force field (EEF) simulation, respectively; (C) Ca^{2+} (blue dot) contacts to SF domain II and another Ca^{2+} (hotpink) contacts to SF domain IV for α_1I at the end of EEF simulation; (D) Ca^{2+} interacts with T^{2p921}, Q^{2p922}, and D^{2p924} from α_1G domain II at t = 0.2 ns in steering molecular dynamics (SMD) simulation; (E) Ca^{2+} interacts with T^{2p874}, I^{2p872}, and Q^{2p875} from α_1H domain II at t = 0.8 ns in SMD simulation; (F) Ca^{2+} interacts with T^{2p742}, Q^{2p743} from α_1I domain II, and K^{3p1302} from α_1I domain II at t = 0.5 ns in SMD simulation.

is smaller than 10 Å. Our SMD tests find T^{2p921}, Q^{2p922}, and D^{2p924} at domain II from α_1G; T^{2p874}, I^{2p872}, and Q^{2p875} at domain II from α_1H; T^{2p742}, Q^{2p743} at domain II; and K^{3p1302} at domain III from α_1I can interact with pulling Ca^{2+} due to the short atom–atom distance (Figure 5D–F). During the 3 ns SMD simulation, a maximum pulling force is less than −15 pN along the z-axis for all three TCCs structures. The reaction coordinate in the tests is fixed in the negative direction along the z-axis; three clusters have different initial z-coordinate of Ca^{2+}, which yield the varied initial force profile. For all three TCC structures, throughout the Ca^{2+} penetration, the absolute value of interatomic force first decreases in the SF region, the increase when Ca^{2+} wants to escape from the SFs. Eventually, it reaches the

maximum before leaving the intercellular gate. Expect for cluster 1s at α_1H and α_1I, an arch-shape force was generated when Ca^{2+} moving towards the negative direction of *Z* (Figure 6).

Replace K^{3p1462} in α_1G with Phe or Gly will shift the activation and decrease the drug sensitivity.[19] FEP analysis finds in water a mutation caused total Gibbs-free energy to increase by 43.83, 40.52, and 36.9 kcal/mol on α_1G, α_1H, and α_1I, respectively. In vacuum, these numbers become 73.96, 43.58, and 62.27 kcal/mol on α_1G, α_1H, and α_1I, respectively. Thus, the contribution of mutation lysine (K^{3p1462}, K^{3p1405}, and K^{3p1302}) at P-loop domain III on whole protein hydration-free energy $\Delta\Delta G_{(K\text{-}A)}$ yields: −30.13, −3.06, and −25.37 kcal/mol. FEP analysis on T^{2p921}, T^{2p874}, and T^{2p742} also finds the polarity of threonine in response to the mutation test. In water, ΔG variation is 13.08, −25.47, and 14.65 kcal/mol for α_1G, α_1H, and α_1I, respectively. These numbers become 13.8, 11.46, and 14.54 kcal/mol (Table 2). Details of how Gibbs-free energy in response to selection of λ during the alchemical reaction in water or vacuum are given in Figure S6. The quality control of FEP analysis is given in Figure S7.

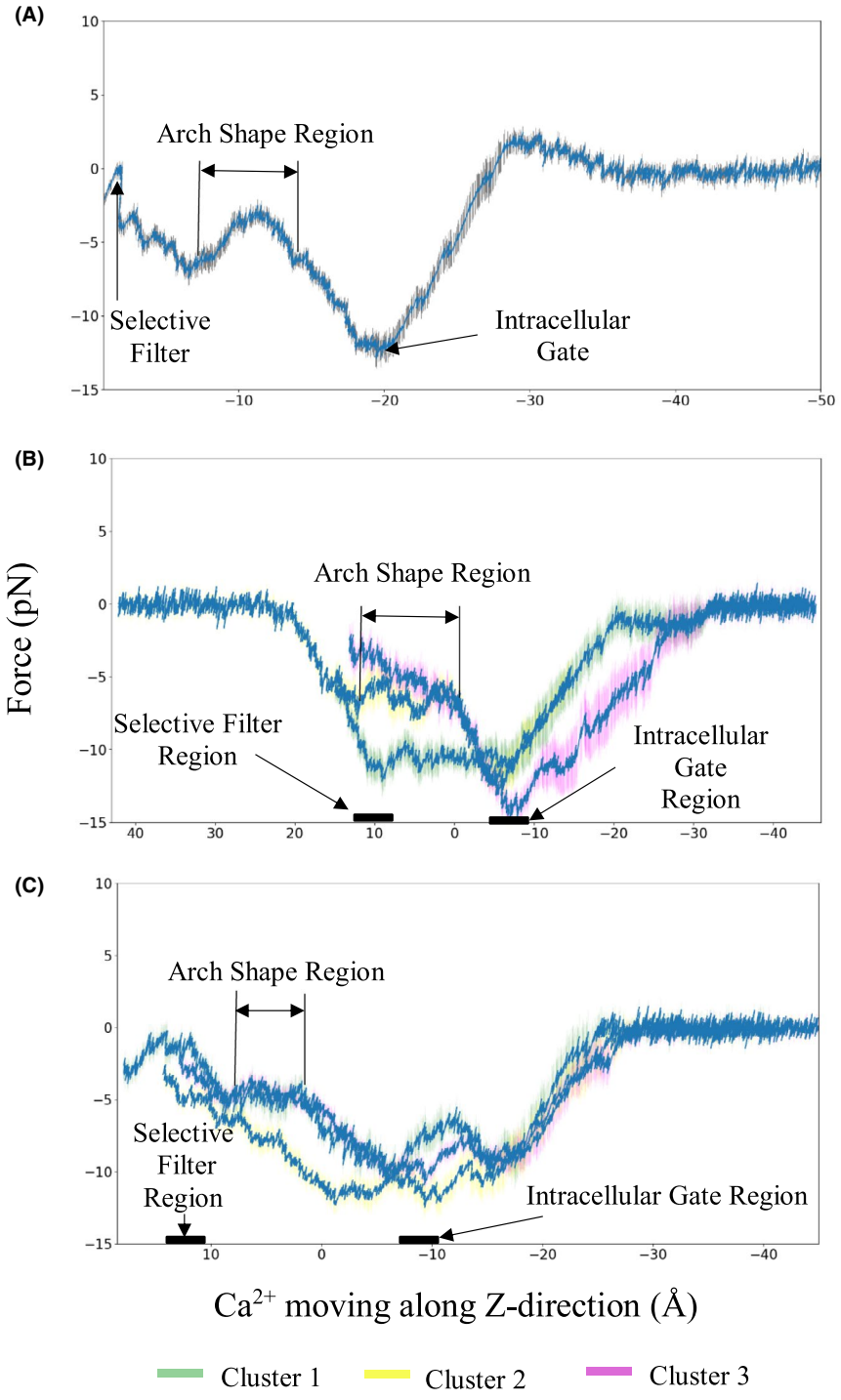

FIGURE 6 Nonlinear increased pulling force (blue) in response to moving one Ca^{2+} across three channels, (A) α_1G, (B) α_1H, and (C) α_1I. The error bar is colored by gray for α_1G and green for selected cluster 1 structure, yellow for selected cluster 2 structure, and magenta for selected cluster 3 structure from last 50 ns of external electric force field (EEF) molecular dynamics (MD) simulation trajectory of α_1H, and α_1I.

TABLE 2 Free Gibbs energy (ΔG) and free hydration energy (ΔΔG) variation introduced by mutation lysine/threonine into alanine (unit: kcal/mol).

	K1462/K1405/K1302			T921/T874/T742		
	$\Delta G_{(Water)}$	$\Delta G_{(Vacuum)}$	ΔΔG	$\Delta G_{(Water)}$	$\Delta G_{(Vacuum)}$	ΔΔG
α_1G	43.83	73.96	−30.13	13.08	13.8	−0.72
α_1H	40.52	43.58	−3.06	−25.47	11.46	−36.93
α_1I	36.9	62.27	−25.37	14.65	14.54	0.11

4 | DISCUSSION

Emerging evidence points out the pathological role of TCCs that is associated with the progression of different diseases. Previous works suggest that nitrile and isopropyl groups in phenylalkylamine serve a role to guide the drug to the position of Ca^{2+}; this function remains positive if the nitrile is replaced with other high electronegative potential elements such as oxygen or sulfur.[42] The recently deposited crystallization structure of human $Ca_v3.1$ offers a great opportunity to explore the Ca^{2+} binding mechanism on all TCCs.[19]

It is suggested that at least 20,000 decoys should be generated if we go through the de novo homology modeling process.[43] Using the human $Ca_v3.1$ structure as a template, we set the sampling number at 15,000 for each comparative modeling case. Although the homology modeling template is constructed based on the splice variant containing a deletion of amino acids within the I–II liker, there are not AAs breaks from SF to the intercellular gates. Therefore, delete the regions that are not aligned with α_1G from selected clustering results should not affect the docking preference of Ca^{2+} to α_1H and α_1I.

Vina does predict binding free energy between ligand and receptor less accurate than MM-PBSA.[44] However, it gives a direct visualization for filtering out the incorrect binding poses between ligand and receptor. Using the predefined homology models, we confirmed that the mibefradil and NNC 55-0396 have different binding regions on the same structure but consistent binding regions from α_1H to α_1I. This finding partially explained why NNC 55-0396 is an exclusive TCCs blocker.[14] The existence of positively charged lysine at P-loop domain III will largely reduce the probability of Ca^{2+} binds to SF at domain III. Our MD simulations further confirmed that SF at P-loop domain II is the common region to dock Ca^{2+} across all TCCs structure. Two AAs (K^{3p1462}/T^{2p921}) that affect the binding affinity of z944 on α_1G[19] also show a clear variation of free hydration energy if mutate to alanine in water. Additional tests results for free hydration energy variation due to the mutation of calcium-binding associated amino acids are available upon request. We used water as solvation in FEP analysis because only K^{3p1462} has a direct impact on α_1G current and conductance. More sophisticated conditions should add into solvate for calculating the influence of polarized AA if it has the potential to be the target site to bind.

DISCLOSURE

The authors declare that the research was conducted in the absence of any commercial or financial relationships that could be construed as a potential conflict of interest.

AUTHOR CONTRIBUTIONS

YL, GYL, and ZC: Design, programming, and writing; KZ, A.E., ML, NZ: Supervision.

ETHICS

N/A.

OPEN RESEARCH BADGES

This article has earned Open Data, Open Materials and Preregistered Research Design badges. Data, materials and the preregistered design and analysis plan are available in the article.

DATA AVAILABILITY STATEMENT

Human $Ca_v3.1$(6KZO), rabbit $Ca_v1.1$ (3JBR), and bacterial Ca_vAb (5KMH) Cryo-EM structures were downloaded from RCSB PDB. Amino acid sequences of $Ca_v3.2$ (O95180) and $Ca_v3.3$ (Q9P0X4) were downloaded from UniProt. The 2D structures of mibefradil and NNC 55-0396 were downloaded from PubChem. The homology modeling and MD simulation data are available on request from the authors.

ORCID

You Lu https://orcid.org/0000-0002-6815-6568

REFERENCES

1. Ivanov AI, Calabrese RL. Intracellular Ca^{2+} dynamics during spontaneous and evoked activity of leech heart interneurons: low-threshold Ca currents and graded synaptic transmission. *J Neurosci*. 2000;20(13):4930-4943.
2. Pan Z-H, Hu H-J, Perring P, Andrade R. T-type Ca^{2+} channels mediate neurotransmitter release in retinal bipolar cells. *Neuron*. 2001;32(1):89-98.
3. Carabelli V, Marcantoni A, Comunanza V, et al. Chronic hypoxia up-regulates α1H T-type channels and low-threshold catecholamine secretion in rat chromaffin cells. *J Physiol*. 2007;584(1):149-165.
4. Tang A-H, Karson MA, Nagode DA, et al. Nerve terminal nicotinic acetylcholine receptors initiate quantal GABA release from perisomatic interneurons by activating axonal T-type (Cav3) Ca^{2+} channels and Ca^{2+} release from stores. *J Neurosci*. 2011;31(38):13546-13561.
5. Yang T, He M, Zhang H, Barrett PQ, Hu C. L-and T-type calcium channels control aldosterone production from human adrenals. *J Endocrinol*. 2020;244(1):237-247.
6. Destefano MB, Stern JS, Castonguay TW. Effect of chronic insulin administration on food intake and body weight in rats. *Physiol Behav*. 1991;50(4):801-806.
7. Ferron L, Capuano V, Ruchon Y, Deroubaix E, Coulombe A, Renaud J-F. Angiotensin II signaling pathways mediate expression of cardiac T-type calcium channels. *Circ Res*. 2003;93(12):1241-1248.
8. Li Y, Tatsui CE, Rhines LD, et al. Dorsal root ganglion neurons become hyperexcitable and increase expression of voltage-gated

T-type calcium channels (Cav3. 2) in paclitaxel-induced peripheral neuropathy. *Pain*. 2017;158(3):417-429.
9. Keyser B, Taylor J, Choi S, et al. Role of T-type Ca^{2+} channels in basal [Ca^{2+}] i regulation and basal insulin secretion in rat islet cells. *Curr Trend Endocrinol*. 2014;7:35-44.
10. Pfeifer MA, Halter JB, Porte D Jr. Insulin secretion in diabetes mellitus. *Am J Med*. 1981;70(3):579-588.
11. Asfaw TN, Tyan L, Glukhov AV, Bondarenko VE. A compartmentalized mathematical model of mouse atrial myocytes. *Am J Physiol-Heart Circ Physiol*. 2020;318(3):H485-H507.
12. Lauzadis J, Liu H, Lu Y, Rebecchi MJ, Kaczocha M, Puopolo M. Contribution of T-type calcium channels to spinal cord injury-induced hyperexcitability of nociceptors. *J Neurosci*. 2020;40(38):7229-7240.
13. Tang L, Gamal El-Din TM, Swanson TM, et al. Structural basis for inhibition of a voltage-gated Ca^{2+} channel by Ca^{2+} antagonist drugs. *Nature*. 2016;537(7618):117-121.
14. Li M, Hansen JB, Huang L, Keyser BM, Taylor JT. Towards selective antagonists of T-type calcium channels: design, characterization and potential applications of NNC 55-0396. *Cardiovasc Drug Rev*. 2005;23(2):173-196.
15. Mullins ME, Horowitz BZ, Linden DH, Smith GW, Norton RL, Stump J. Life-threatening interaction of mibefradil and β-blockers with dihydropyridine calcium channel blockers. *JAMA*. 1998;280(2):157-158.
16. Tringham E, Powell KL, Cain SM, et al. T-type calcium channel blockers that attenuate thalamic burst firing and suppress absence seizures. *Sci Transl Med*. 2012;4(121):121ra19.
17. Casillas-Espinosa PM, Hicks A, Jeffreys A, Snutch TP, O'Brien TJ, Powell KL. Z944, a novel selective T-type calcium channel antagonist delays the progression of seizures in the amygdala kindling model. *PLoS One*. 2015;10(8):e0130012.
18. LeBlanc BW, Lii TR, Huang JJ, et al. T-type calcium channel blocker Z944 restores cortical synchrony and thalamocortical connectivity in a rat model of neuropathic pain. *Pain*. 2016;157(1):255-263.
19. Zhao Y, Huang G, Wu Q, et al. Cryo-EM structures of apo and antagonist-bound human Ca v 3.1. *Nature*. 2019;576(7787):492-497.
20. Song Y, DiMaio F, Wang R-R, et al. High-resolution comparative modeling with RosettaCM. *Structure*. 2013;21(10):1735-1742.
21. Rohl CA, Strauss CE, Misura KM, Baker D. Protein structure prediction using Rosetta. *Methods Enzymol*. 2004;383:66-93.
22. Laskowski RA, MacArthur MW, Moss DS, Thornton JM. PROCHECK: a program to check the stereochemical quality of protein structures. *J Appl Crystallogr*. 1993;26(2):283-291.
23. Hooft RW, Vriend G, Sander C, Abola EE. Errors in protein structures. *Nature*. 1996;381(6580):272.
24. O'Boyle NM, Banck M, James CA, Morley C, Vandermeersch T, Hutchison GR. Open Babel: an open chemical toolbox. *J Cheminformatics*. 2011;3(1):33.
25. Miteva MA, Guyon F, Tuffery P. Frog2: efficient 3D conformation ensemble generator for small compounds. *Nucleic Acids Res*. 2010;38(Web Server):W622-W627.
26. Trott O, Olson AJ. AutoDock Vina: improving the speed and accuracy of docking with a new scoring function, efficient optimization, and multithreading. *J Comput Chem*. 2010;31(2):455-461.
27. Lee J, Hitzenberger M, Rieger M, Kern NR, Zacharias M, Im W. CHARMM-GUI supports the Amber force fields. *J Chem Phys*. 2020;153(3):035103.
28. Kim S, Lee J, Jo S, Brooks CL III, Lee HS, Im W. CHARMM-GUI ligand reader and modeler for CHARMM force field generation of small molecules. *J Comput Chem*. 2017;38(21):1879-1886.
29. Bhattacharjee A, Whitehurst RM Jr, Zhang M, Wang L, Li M. T-type calcium channels facilitate insulin secretion by enhancing general excitability in the insulin-secreting β-cell line, INS-1. *Endocrinology*. 1997;138(9):3735-3740.
30. Wu S, Haynes J Jr, Taylor JT, et al. Cav3. 1 (α1G) T-type Ca^{2+} channels mediate vaso-occlusion of sickled erythrocytes in lung microcirculation. *Circ Res*. 2003;93(4):346-353.
31. Charrad M, Ghazzali N, Boiteau V, Niknafs A, Charrad MM. Package 'nbclust'. *J Stat Softw*. 2014;61:1-36.
32. Scheurer M, Rodenkirch P, Siggel M, et al. PyContact: rapid, customizable, and visual analysis of noncovalent interactions in MD simulations. *Biophys J*. 2018;114(3):577-583.
33. Hénin J, Gumbart J, Chipot C. In silico alchemy: a tutorial for alchemical free-energy perturbation calculations with NAMD. see www ks uiuc edu/Training/Tutorials/namd/FEP/tutorial-FEP pdf for the NAMD software. 2017.
34. Pohorille A, Jarzynski C, Chipot C. Good practices in free-energy calculations. *J Phys Chem B*. 2010;114(32):10235-10253.
35. Liu P, Fo D, Cai W, Chipot C. A toolkit for the analysis of free-energy perturbation calculations. *J Chem Theory Comput*. 2012;8(8):2606-2616.
36. Harding SD, Sharman JL, Faccenda E, et al. The IUPHAR/BPS Guide to PHARMACOLOGY in 2018: updates and expansion to encompass the new guide to IMMUNOPHARMACOLOGY. *Nucleic Acids Res*. 2018;46(D1):D1091-D1106.
37. Armstrong JF, Faccenda E, Harding SD, et al. The IUPHAR/BPS Guide to PHARMACOLOGY in 2020: extending immunopharmacology content and introducing the IUPHAR/MMV Guide to MALARIA PHARMACOLOGY. *Nucleic Acids Res*. 2020;48(D1):D1006-D1021.
38. Heady TN, Gomora JC, Macdonald TL, Perez-Reyes E. Molecular pharmacology of T-type Ca^{2+} channels. *Jpn J Pharmacol*. 2001;85(4):339-350. https://doi.org/10.1254/jjp.85.339
39. Chen Y, Parker WD, Wang K. The role of T-type calcium channel genes in absence seizures. *Front Neurol*. 2014;5:45. https://doi.org/10.3389/fneur.2014.00045
40. Lu Y, Li M. A new computer model for evaluating the selective binding affinity of phenylalkylamines to T-Type Ca^{2+} channels. *Pharmaceuticals*. 2021;14(2):141.
41. Yao X-Q, Grant BJ. Domain-opening and dynamic coupling in the α-subunit of heterotrimeric G proteins. *Biophys J*. 2013;105(2):L08-L10.
42. Cheng RC, Tikhonov DB, Zhorov BS. Structural model for phenylalkylamine binding to L-type calcium channels. *J Biol Chem*. 2009;284(41):28332-28342.
43. Bender BJ, Cisneros A, Duran AM, et al. Protocols for molecular modeling with Rosetta3 and RosettaScripts. *Biochemistry*. 2016;55(34):4748-4763.
44. Genheden S, Ryde U. The MM/PBSA and MM/GBSA methods to estimate ligand-binding affinities. *Expert Opin Drug Discov*. 2015;10(5):449-461.

SUPPORTING INFORMATION

Additional supporting information may be found online in the Supporting Information section.

How to cite this article: Lu Y, Li M, Lee GY, et al. Seeking the exclusive binding region of phenylalkylamine derivatives on human T-type calcium channels via homology modeling and molecular dynamics simulation approach. *Pharmacol Res Perspect*. 2021;9:e00783. https://doi.org/10.1002/prp2.783